

Article

Crystal Structure, Hirshfeld Surface Analysis, and Computational Study of Quinolin-8-yl 4-Chlorobenzoate: Insights from Spectroscopic, Thermal, and Antitumor Properties

Juan-Carlos Castillo ^{1,*} , Diana Becerra ¹  and Mario A. Macías ^{2,*} 

¹ Escuela de Ciencias Química, Universidad Pedagógica y Tecnológica de Colombia, Avenida Central del Norte 39-115, Tunja 150003, Colombia; diana.becerra08@uptc.edu.co

² Crystallography and Chemistry of Materials, Department of Chemistry, Universidad de los Andes, Carrera 1 No. 18A-10, Bogotá 111711, Colombia

* Correspondence: juan.castillo06@uptc.edu.co (J.-C.C.); ma.maciasl@uniandes.edu.co (M.A.M.); Tel.: +57-8-740-5626 (ext. 2425) (J.-C.C.); +57-60-1-339949 (ext. 1482) (M.A.M.)

Abstract: We report the time-efficient synthesis of quinolin-8-yl 4-chlorobenzoate (**3**) via an *O*-acylation reaction between 8-hydroxyquinoline (**1**) and 4-chlorobenzoyl chloride (**2**) mediated by triethylamine in acetonitrile under heating at 80 °C for 20 min in the Monowave 50 reactor. This protocol is distinguished by its short reaction time, operational simplicity, and clean reaction profile. The structure of **3** was fully characterized through a combination of analytical techniques, including NMR, IR, and UV-Vis spectroscopy, MS spectrometry, differential scanning calorimetry (DSC), thermogravimetry (TG), and crystallographic studies. Interestingly, X-ray diffraction analyses of **3** show that the crystal structure is characterized by C-H...N, C-H...O, Cl... π , and π ... π interactions. The molecular conformation presents an orthogonal orientation between aromatic rings in the solid state. The calculated interaction energies using the CE-B3LYP model show that dispersion forces act in a higher proportion to build the crystal, which is consistent with the few short hydrogen interactions detected. Electrostatic potential maps suggest the formation of σ -holes over the Cl atoms. Although they can behave as both Lewis acid and base sites, Cl...Cl interactions are absent due to the shallow depth of these σ -holes. Quantum chemical descriptors and global reactivity descriptors were examined using the B3LYP method with the 6-31G(d,p) basis set implemented in CrystalExplorer. Finally, compound **3** exhibited low activity against HOP-92 and EKVX non-Small-cell lung and UO-31 Renal cancer cell lines, with a growth inhibition percentage (GI%) ranging from 6.2% to 18.1%.

Keywords: 8-hydroxyquinoline; X-ray crystallography; Hirshfeld surface maps; molecular orbitals; cancer



Citation: Castillo, J.-C.; Becerra, D.; Macías, M.A. Crystal Structure, Hirshfeld Surface Analysis, and Computational Study of Quinolin-8-yl 4-Chlorobenzoate: Insights from Spectroscopic, Thermal, and Antitumor Properties. *Crystals* **2023**, *13*, 694. <https://doi.org/10.3390/cryst13040694>

Academic Editor: Josefina Perles

Received: 27 March 2023

Revised: 11 April 2023

Accepted: 12 April 2023

Published: 18 April 2023



Copyright: © 2023 by the authors. Licensee MDPI, Basel, Switzerland. This article is an open access article distributed under the terms and conditions of the Creative Commons Attribution (CC BY) license (<https://creativecommons.org/licenses/by/4.0/>).

1. Introduction

Quinoline consists of a pyridine fused with a benzene ring at two adjacent carbon atoms. It is a weak tertiary base (pK_b of 4.85) that shows both electrophilic and nucleophilic substitution reactions with analogs to benzene and pyridine [1]. Synthetic and naturally occurring quinolines have been used as potent pharmacophores due to their wide range of biological activities, such as anti-malarial [2], antibacterial [3], antiviral [4], antifungal [5], antipsychotic [6], anti-inflammatory [7], analgesic [7], anti-asthmatic [8], anti-leishmanial [9], and anti-hypertensive activities [10]. Modern medicinal chemistry is significantly impacted by quinoline analogues, which have resulted in several anticancer drugs that are either commercially available on the market or in different stages of clinical trials involving different mechanisms of action [11–16]. A significant number of protein kinase inhibitors are based on quinoline (Figure 1), including cabozantinib (Cabometyx[®]) used for the treatment of advanced renal cell carcinoma (RCC) and medullary thyroid carcinoma (MTC), which acts as a multi-targeted tyrosine kinase inhibitor, including vascular endothelial growth factor receptor 2 (VEGFR2), hepatocyte growth factor receptor

(c-MET/HGFR), and proto-oncogene tyrosine-protein kinase receptor (RET) [12,17], bosutinib is employed to treat the chronic myelogenous leukemia (CML), which act as a strong inhibitor of Bcr-Abl kinase [12,18], and lenvatinib is used to treat the thyroid cancer and in combination with other medicines to treat advanced renal cell carcinoma (RCC) and hepatocellular carcinoma (HCC), acting as a multi-targeted kinase inhibitor against vascular endothelial growth factor receptors (VEGFR 1–3), fibroblast growth factor receptors (FGFR 1–4), and platelet-derived growth factor receptors (PDGF-R) [12,19]. There are relevant quinoline-based topoisomerase inhibitors, including camptothecin (CPT), that act as inhibitors of DNA topoisomerase I; however, it has a poor pharmacokinetic profile, including low stability and solubility (Figure 1) [11]. The α -hydroxy lactone ring (E-ring) constitutes the most critical component of its structure, which engages with the topoisomerase enzyme through one hydrogen bond of the hydroxy group in position 20 with Asp533, alongside two hydrogen bonds of the lactone with amino groups on Arg364 [11]. To address the limitations of camptothecin, numerous semisynthetic derivatives of CPT have been effectively synthesized so far. Figure 1 illustrates that irinotecan is effective in treating Colorectal cancer, whereas topotecan is used to treat Small-cell lung, Cervical, and Ovarian cancers [20].

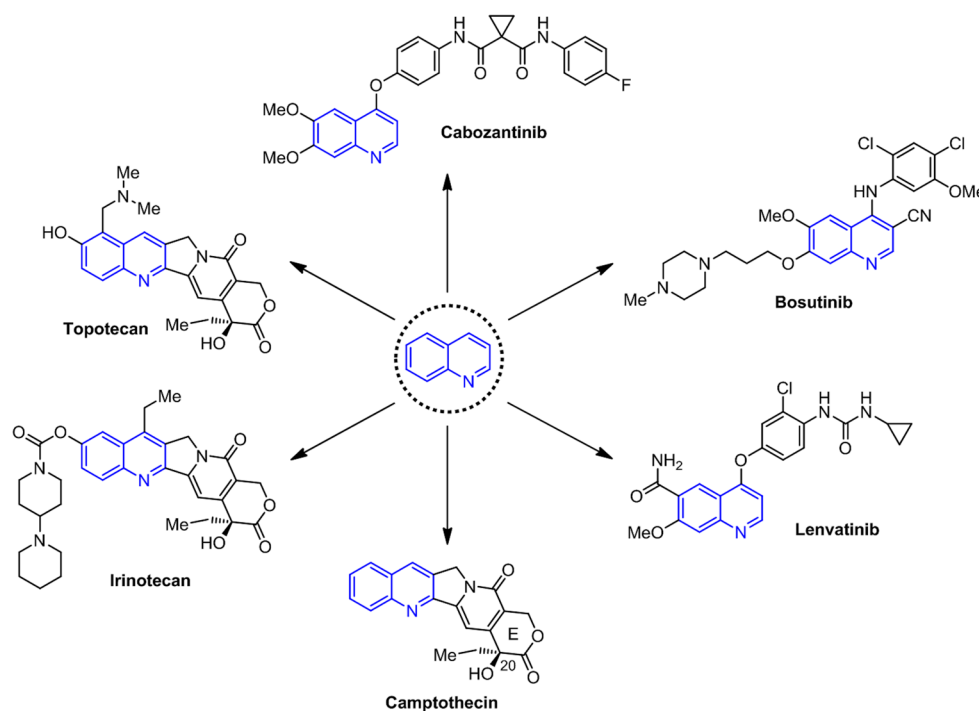


Figure 1. Some important quinoline-containing anticancer drugs.

The varied physical, chemical, and biological characteristics exhibited by a certain set of quinoline derivatives have made them a subject of considerable interest in drug design and medicinal chemistry for the past two decades [21–23]. In particular, clioquinol and nitroxoline are the most well-known 8-hydroxyquinoline derivatives due to their broad range of targets. For instance, nitroxoline displayed more potent anticancer activity with an IC_{50} of 5–10 fold less than clioquinol [24]. In vitro and in vivo studies confirmed that nitroxoline acted as an antiangiogenic agent [25]. It should be noted that biological properties are much broader and cover antiviral [23], anti-mycobacterial [23], antiprotozoal [23], anti-neurodegenerative [23], antimicrobial [26], analgesic [27], anti-asthmatic [27], and anticancer [22,23], among other activities. In addition, the position of the hydroxyl group in close proximity to the pyridine core renders 8-hydroxyquinoline derivatives significant bidentate chelating agents, capable of forming complexes with a diverse range of metal ions [28–31]. Over the past few years, there has been a modest exploration of

the functionalization of the hydroxyl group situated at position 8 of the quinoline framework. A search in the Reaxys database showed three different synthetic approaches to prepare quinolin-8-yl 4-chlorobenzoate (**3**), with up to 84% yield using solvents such as dichloromethane, *N,N*-dimethylformamide, and toluene, and bases such as potassium carbonate and triethylamine, under stirring at room temperature or heating at 120 °C for reaction times ranging from 20 min to 6 h [32–34]. It is interesting to note that the X-ray crystallography of this compound was not present in the Cambridge Structural Database (CSD) when searched using the ConQuest software. Hence, an analysis of spectroscopic, thermal, and X-ray crystallographic data was conducted in this study to obtain valuable insights. Additionally, the synthesis of **3** was performed utilizing a Monowave 50 reactor through a triethylamine-mediated *O*-acylation reaction involving the precursors **1** and **2** in acetonitrile at 80 °C for 20 min. Lastly, anticancer studies of **3** were screened against 60 human cancer cell lines by the National Cancer Institute (NCI, Germantown, MD, USA).

2. Materials and Methods

2.1. General Information

The reactions were followed by Thin Layer Chromatography (TLC) and analyzed by a UV lamp (254 or 365 nm). ¹H and ¹³C NMR spectra were recorded in CDCl₃ at 298 K on a Bruker Avance 400 spectrophotometer operating at 400.1 and 100.6 MHz, respectively. ¹H and ¹³C NMR spectra were processed using as internal standards the residual non-deuterated signal ($\delta = 7.26$ ppm) and the deuterated solvent signal ($\delta = 77.16$ ppm), respectively. IR spectra were obtained using a Shimadzu FTIR 8400 spectrophotometer equipped with an ATR accessory, operating at room temperature. A methanol solution (50 μ M) was utilized to obtain the UV–Vis spectra using an Evolution 201 UV–Vis spectrophotometer. Differential scanning calorimetry (DSC) and thermogravimetric analysis (TGA) were performed in a thermogravimetry/differential thermal analyzer STA7200. By conducting microanalyses with a CHNS elemental analyzer, we found that the measured values were consistent with the theoretical values within a range of $\pm 0.4\%$. A direct inlet probe operating at 70 eV was used in the SHIMADZU-GCMS 2010-DI-2010 spectrometer to collect the mass spectra. All reactions were conducted in a reactor, Monowave 50, employing a borosilicate glass vial (10 mL) with a silicone cap [35]. The reaction vessel's temperature contact sensor situated at the cavity bottom. The X-ray diffraction data were obtained at ambient temperature, 298 (2) K, using MoK α radiation ($\lambda = 0.71073$ Å) and measurements of ω scans in an Agilent SuperNova, Dual, Cu at Zero, Atlas four-circle diffractometer equipped with a CCD plate detector. The collected frames were integrated with the CrysAlis PRO software package [36]. Absorption correction was performed by the CrysAlis PRO software package using the empirical absorption correction, implemented in the SCALE3 ABSPACK scaling algorithm [36]. The structure of **3** was solved using an iterative algorithm [37] and then completed by a different Fourier map.

2.2. Synthesis of Quinolin-8-yl 4-Chlorobenzoate (**3**)

A mixture of starting materials **1** (72 mg, 0.50 mmol) and **2** (64 μ L, 0.50 mmol) in the presence of Et₃N (84 μ L, 0.60 mmol) in CH₃CN (2.0 mL) were added in a processing vial (10 mL) equipped with a magnetic stir bar. The Monowave 50 reactor was used to heat the reaction mixture at 80 °C with a 20 min hold time and stirred at 600 rpm in AFAP mode (As Fast As Possible). The reaction mixture was cooled, the solvent was eliminated under reduced pressure, and the resulting reaction mixture was purified by column chromatography on silica gel using a mixture of dichloromethane/*n*-hexane (2:1, *v/v*) as an eluent to give the desired compound **3** as colorless needles (129 mg, 91% yield). Under normal pressure and ambient temperature, compound **3** was subjected to recrystallization in methanol to obtain colorless prisms. R_f (CH₂Cl₂) = 0.65. M.p. 162 °C. FTIR–ATR: $\nu = 3086, 3036, 1730$ (ν C=O), 1627 (ν C=N), 1593 (ν C=C), 1490 (ν C=C), 1404 (ν C–C), 1387 (ν C–C), 1370 (ν C–C), 1287 (ν C–N and ν C–C), 1258 (ν C–C(=O)–O and ν C–N), 1231, 1176, 1160, 1087 (ν O–C–C), 1064, 1042, 1007, 854, 820, 794, 760 (ν C–Cl), 706, 680,

525 cm^{-1} . UV-Vis (methanol) λ_{max} (ϵ , $\text{L}\cdot\text{mol}^{-1}\cdot\text{cm}^{-1}$): 205 (47,000, $\pi \rightarrow \pi^*$), 229 (49,600, $\pi \rightarrow \pi^*$), 243 (26,400, $\pi \rightarrow \pi^*$), 278 (8400, $n \rightarrow \pi^*$) nm. ^1H NMR (400 MHz, CDCl_3): δ = 7.43 (dd, J = 8.2, 4.2 Hz, 1H, H-3), 7.52 (d, J = 8.8 Hz, 2H, H_m), 7.55–7.61 (m, 2H, H-6, H-7), 7.78 (dd, J = 7.2, 2.4 Hz, 1H, H-5), 8.20 (dd, J = 8.4, 1.2 Hz, 1H, H-4), 8.29 (d, J = 8.8 Hz, 2H, H_o), 8.88 (dd, J = 4.0, 1.6 Hz, 1H, H-2) ppm. $^{13}\text{C}\{^1\text{H}\}$ NMR (101 MHz, CDCl_3): δ = 121.6 (CH, C-7), 121.9 (CH, C-3), 126.3 (CH, C-5), 126.4 (CH, C-6), 128.1 (C, C_i), 129.1 (2CH, C_m), 129.7 (C, C-4a), 132.1 (2CH, C_o), 136.1 (CH, C-4), 140.2 (C, C_p), 141.4 (C, C-8a), 147.7 (C, C-8), 150.8 (CH, C-2), 164.8 (C, C=O) ppm. Anal. calcd. for $\text{C}_{16}\text{H}_{10}\text{ClNO}_2$ (283.70): C, 67.74; H, 3.55; N, 4.94. Found: C, 67.97; H, 3.57; N, 4.96. MS (EI, 70 eV) m/z (%): 285/283 (4/12) [$\text{M}^+\bullet$], 141/139 (33/100), 113/111 (15/44), 69 (30), 57 (23), 43 (22).

2.3. Refinement and Data Collection Strategy

The presentation of crystallographic data and refinement details can be found in Table 1. The refinement process involved the anisotropic nature of non-hydrogen atoms. Meanwhile, hydrogen atoms were added geometrically at a distance of 0.93 Å from carbon and refined as riding contributions. This process was carried out using isotropic displacement parameters, which were set at 1.2 times the U_{eq} value of the parent atom. The refinement of crystal structure was executed using SHELXL2018/3 [38], and Mercury [39] was employed to perform molecular and supramolecular graphics.

Table 1. Crystallographic data of compound 3.

Crystal Data	Compound 3
CCDC	2,241,325
Chemical formula	$\text{C}_{16}\text{H}_{10}\text{ClNO}_2$
Mr	283.70
Solvent for crystallization	Methanol
Crystalline system, space group	Monoclinic, $P2_1/c$
a, b, c (Å)	12.0532 (14), 13.3785 (17), 8.4098 (13)
α , β , γ ($^\circ$)	90, 98.392 (13), 90
Volume, (Å ³)	1341.6 (3)
ρ , kg m^{-3}	1.405
Z	4
Temperature, (K)	298 (2)
Radiation type	Mo $K\alpha$
μ (mm^{-1})	0.28
Theta range for data collection	$3.045^\circ < 2\theta < 26.368^\circ$
Index range	$-15 \leq h \leq 15$, $-16 \leq k \leq 16$, $-10 \leq l \leq 10$
Data collection	
Diffractometer	SuperNova, Dual, Cu at zero, Atlas Multi-Scan method
Absorption correction	CrysAlis PRO 1.171.41.119a (Rigaku Oxford Diffraction, 2021)
Tmin, Tmax	0.503, 1.000
No. of measured, independent and observed reflections [$I > 2\sigma(I)$]	14,107, 2744, 2176
Rint	0.050
($\sin \theta / \lambda$) max (Å ⁻¹)	0.625
Refinement	
$R[F^2 > 2\sigma(F^2)]$, wR(F^2), S	0.045, 0.128, 1.06
No. of reflections	2744
Refined parameters	182
No. of restraints	0
H-atoms treatment	H-atom parameters constrained
$\Delta\rho_{\text{max}}$, $\Delta\rho_{\text{min}}$ ($\text{e}\text{Å}^{-3}$)	0.17, -0.37

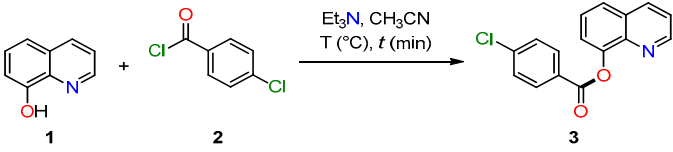
2.4. Computational Methods

The crystallographic information contained in the cif (crystallographic information file) file was used to perform computational calculations. Hirshfeld (HF) surfaces mapped over d_{norm} were used to investigate the close contacts further [40]. Electrostatic potentials mapped on HS were calculated employing the program TONTO by the B3LYP method with the 6-31G(d,p) basis set [41,42]. Energy frameworks were computed based on CE-B3LYP interaction energies (kJ mol^{-1}) using the B3LYP method with the 6-31G(d,p) basis set [43]. The models in *CrystalExplorer* were used to calculate molecular pair energies [44], which are depicted with cylinders connecting molecular centroids (radii proportional to the magnitude of the interaction). Quantum chemical (frontier molecular orbitals and HOMO-LUMO energy gap) and global reactivity descriptors were calculated by the B3LYP method and 6-31G(d,p) basis set, using *CrystalExplorer*. TONTO program was utilized to perform these calculations.

3. Results and Discussion

3.1. Chemistry

The synthesis of heteroaromatic esters is often achieved through the esterification reactions of acyl chlorides and hydroxyheteroaromatic compounds [45,46]. This chemical transformation has been widely applied in the pharmaceutical industry, organic chemistry, and material science due to its operational efficiency, reduced reaction times, and the fact that the starting materials are economical and commercially available [45,46]. Over the past twenty years, three distinct synthetic strategies have been reported for the synthesis of quinolin-8-yl 4-chlorobenzoate (**3**), yielding up to 84% under various solvents such as dichloromethane, *N,N*-dimethylformamide, and toluene, and different bases such as potassium carbonate and triethylamine, stirring at room temperature and heating at 120 °C for reaction times ranging from 20 min to 6 h [32–34]. Reaxys and CSD databases do not show information about its IR and UV–Vis spectra, thermal behavior, single-crystal X-ray diffraction, or anticancer studies. Moreover, we use the Monowave 50 reactor as an alternative protocol for the synthesis of quinoline-containing ester **3** under mild reaction conditions. Recently, Kappe's group studied some relevant organic transformations with the conductively heated Monowave 50 reactor, finding that in most cases the reaction time, stirring efficiency, yield, heating, and cooling performance are similar to the results obtained with a standard microwave apparatus [47]. The Monowave 50 reactor was used to perform the triethylamine-mediated synthesis of compound **3** using equimolar amounts of reactants **1** and **2** in acetonitrile under different temperatures and reaction times (Table 2). The optimum outcome was achieved by heating in AFAP mode at 80 °C with a hold time of 20 min and 600 rpm stirring speed (Entry 1, Table 2). Following the removal of the solvent under reduced pressure, the crude mixture is subjected to flash column chromatography purification to afford quinoline-containing ester **3** with a 91% yield. In Entries 2 and 3, Table 2, the yields of **3** were reduced when the reaction was conducted for 20 min below 80 °C. In Entry 4, Table 2, a decrease in the yield of **3** was observed when the reaction time was shortened from 20 to 10 min at 80 °C. Consistent with expectations, compound **3** was obtained in moderate yield (52%), under conventional heating at 20 °C for 20 min (Entry 5, Table 2). This synthetic approach is distinguished by its short reaction time and operational simplicity and requires a slight excess of base (1.2 equiv), in comparison with previously reported data (2.0 equiv) [33,34]. According to the environmental risk-based ranking of solvents proposed by Tobiszewski's group, solvents that are carcinogenic, toxic, or produce other effects are found in the lower part of the ranking [48]. Importantly, acetonitrile (rank 31) is higher than toluene and dichloromethane (ranks 59 and 61, respectively), which have been used to synthesize compound **3**. Without any discussion, *N,N*-dimethylformamide is treated as an undesirable solvent. Despite the benefits of acetonitrile in the pharmaceutical industry, it has adverse health effects and a relatively poor environmental profile.

Table 2. Synthesis of the quinolin-8-yl 4-chlorobenzoate (**3**)^a.


Entry	Temperature (°C)	Time (min)	Yield 3 (%) ^c
1	80	20	91
2	60	20	88
3	40	20	76
4	80	10	79
5 ^b	20	20	52

^a Reaction conditions: **1** (0.50 mmol), **2** (0.50 mmol), and Et₃N (0.60 mmol) in CH₃CN (2.0 mL) at 40–80 °C for 10–20 min using the Monowave 50 reactor. ^b Absence of the Monowave 50 reactor. ^c The ester was purified by column chromatography.

3.2. NMR Analysis

We analyzed the ¹H and ¹³C NMR spectra of quinolin-8-yl 4-chlorobenzoate (**3**) (Figures S5 and S6). ¹H-NMR spectra displayed three doublets of doublets at 7.43, 8.20, and 8.88 ppm assigned to H-3, H-4, and H-2 protons of the π -deficient pyridine ring, respectively (Figure 2 and Table 3). Furthermore, the H-2 proton is the most deshielded due to its closeness to the pyridinic nitrogen atom. Moreover, the benzene fused to the pyridine ring showed a doublet of doublets at 7.78 ppm associated with the H-5 proton and a multiplet ranging from 7.55 to 7.61 ppm assigned to the H-6 and H-7 protons. Additionally, the ester and chloro groups cause Hm protons (7.52 ppm) to be more shielded compared with Ho protons (8.29 ppm). The absence of a proton signal detected from the hydroxyl group attached to the quinoline ring served as confirmation of the successful O-acylation process. These assignments were also confirmed by the COSY spectrum (Table 3 and Figure S9). The H-2 proton at 8.88 ppm displayed a correlation with a signal at 7.43 ppm, which was identified as the H-3 proton. From this signal, we detected the next correlation at 8.20 ppm, corresponding to the H-4 proton. A COSY cross peak was observed between the H-5 proton at 7.78 ppm and a multiplet ranging from 7.55 to 7.61 ppm, which was assigned to the H-6 and H-7 protons that were strongly coupled to each other. Finally, the Ho proton signal at 8.29 ppm displayed a cross peak with a doublet located at 7.52 ppm, which was identified as the Hm protons. In summary, the COSY technique is in principle sufficient to assign all protons of quinolin-8-yl 4-chlorobenzoate (**3**) with safety.

Analysis of the ¹³C-NMR and DEPT-135 spectra for compound **3** indicated the existence of eight aromatic methines, five quaternary aromatic carbons, and one carbonyl carbon (Figure 2 and Table 3). The HSQC spectrum allowed the assignment of all methine carbons C-7, C-3, C-5, C-6, Cm, Co, C-4, and C-2 at 121.6, 121.9, 126.3, 126.4, 129.1, 132.1, 136.1, and 150.8 ppm, respectively (Figure S7). The assignment of all quaternary carbons Ci, C-4a, Cp, C-8a, C-8, and C=O was performed with the HMBC spectrum (Table 3 and Figure S8). A ³J(C,H) spin coupling was observed between the H-2 and H-3 protons and C-8a (141.4 ppm) and C-4a (129.7 ppm), respectively. Moreover, the aromatic quaternary carbon C-8 (147.7 ppm) is the most deshielded due to its closeness to the oxygen atom, which had a ²J(C,H) spin coupling to the H-7 proton. Analysis of the spectra revealed that the Ho protons exhibited two ³J(C,H) spin couplings with Cp at 140.2 ppm and C=O at 164.8 ppm. Conversely, Ci at 128.1 ppm displayed a single connectivity with Hm protons.

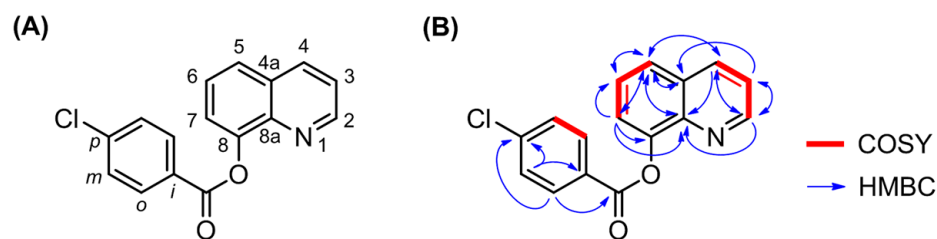


Figure 2. (A) Structure of compound **3**; (B) Correlations of **3** based on COSY and HMBC experiments.

Table 3. NMR assignments and correlations of compound **3** using 1D and 2D experiments.

Number	δ_{H} (mult, J in Hz)	δ_{C} (ppm)	COSY	HMBC
2	8.88 (dd, $J = 4.0, 1.6$)	150.8	H-3 (3J)	C-3 (2J) C-8a (3J) C-4 (3J)
3	7.43 (dd, $J = 8.2, 4.2$)	121.9	H-2 (3J) H-4 (3J)	C-4a (3J) C-2 (2J)
4	8.20 (dd, $J = 8.4, 1.2$)	136.1	H-3 (3J)	C-5 (3J) C-8a (3J) C-2 (3J)
4a	–	129.7	–	–
5	7.78 (dd, $J = 7.2, 2.4$)	126.3	H-6 (3J)	C-4a (2J) C-6 (2J) C-8a (3J) C-4 (3J) C-7 (3J)
6	7.55–7.61 (m)	126.4	H-5 (3J) H-7 (3J)	C-5 (2J) C-8 (3J) C-4a (3J)
7	7.55–7.61 (m)	121.6	H-6 (3J)	C-6 (2J) C-8 (2J) C-8a (3J) C-5 (3J)
8	–	147.7	–	–
8a	–	141.4	–	–
C=O	–	164.8	–	–
i	–	128.1	–	–
o	8.29 (d, $J = 8.8$)	132.1	H _m (3J)	C _p (3J) C=O (3J)
m	7.52 (d, $J = 8.8$)	129.1	H _o (3J)	C _p (2J) C _i (3J)
p	–	140.2	–	–

3.3. Vibrational Analysis

The IR spectrum of **3** is illustrated in Figures S2 and S3. The ester group possesses two asymmetrically coupled vibrations, namely C-C(=O)-O and O-C-C, which appear in the region of 1250–1310 cm^{-1} and 1111 cm^{-1} , respectively [49,50]. For compound **3**, we observed C-C(=O)-O and O-C-C stretching vibrations at 1258 and 1087 cm^{-1} , respectively. Moreover, the C=O stretching vibration of compound **3** was assigned at 1730 cm^{-1} , which is within the typical range of 1715–1730 cm^{-1} for the carbonyl band of α,β -unsaturated and benzoate esters [49,50].

Generally, C=N and C=C stretching bands are observed as combinational bands. In this work, the C=N stretching vibration is observed at 1627 cm^{-1} . In contrast, C–N stretching modes appear in the range of $1200\text{--}1400\text{ cm}^{-1}$, which are overlapped with C–C and C–O vibrations [49,50]. In this regard, Krishnakumar et al. and Bahgat et al. reported C–N stretching vibrations of 8-hydroxyquinoline at $1273/1286\text{ cm}^{-1}$ and $1286/1339\text{ cm}^{-1}$, respectively [51,52], whereas in this study, compound **3** showed C–N stretching bands at 1258 and 1287 cm^{-1} .

The (hetero)aromatic compounds displayed C–H stretching modes in the $3000\text{--}3100\text{ cm}^{-1}$ range [49], whereas in this study, compound **3** exerted C–H stretching bands at 3036 and 3086 cm^{-1} . Furthermore, the out-of-plane (“oop”) bending of aromatic C–H bonds is observed in the $675\text{--}900\text{ cm}^{-1}$ range [49]. In this work, the out-of-plane vibrations of the quinoline ring are assigned at 706 , 820 , and 854 cm^{-1} , while the benzene ring showed another out-of-plane C–H bending vibration at 794 cm^{-1} , confirming the *para*-substitution. Previous studies have reported the in-plane bending vibrations of aromatic C–H bonds in the range of $1000\text{--}1300\text{ cm}^{-1}$ [49]. For compound **3**, we observed these vibrations in benzene and quinoline rings at 1007 , 1042 , 1064 , 1160 , 1176 , and 1231 cm^{-1} .

Vibrational frequencies of C=C bonds in (hetero)aromatic compounds can be found within the $1400\text{--}1600\text{ cm}^{-1}$ range [49]. For example, Fernandes et al. described that the 8-hydroxyquinoline and the 4,7-dichloroquinoline had a C=C stretching vibration at 1578 cm^{-1} [50]. Moreover, Saral et al. described that the 2-chloroquinoline-3-carboxaldehyde had a C=C stretching band at 1612 cm^{-1} [53]. In this work, the C=C stretching modes of compound **3** were identified at 1490 and 1593 cm^{-1} . While the expected range of C–C stretching vibrations is $1250\text{--}1450\text{ cm}^{-1}$, and these vibrations are usually mixed with C–N and C–O vibrations, the present study designates the C–C stretching vibrations of benzene and quinoline rings at 1258 , 1287 , 1370 , 1387 , and 1404 cm^{-1} .

The stretching mode of the C–Cl bond in compound **3** is detected at 760 cm^{-1} , in agreement with previously reported data ($580\text{--}750\text{ cm}^{-1}$) [54]. It could shift to a higher value due to the presence of the ester group.

3.4. UV–Vis Analysis

The study of 8-hydroxyquinoline derivatives remains an intriguing subject due to their innumerable applications in photoluminescence [55], electroluminescence [56], organic photovoltaic devices [57], and selective detection of various metal ions due to their high chelating ability [28–31]. For that reason, we conducted UV–Vis studies for 8-hydroxyquinoline (**1**) and quinolin-8-yl 4-chlorobenzoate (**3**) in the range of $200\text{--}400\text{ nm}$ in methanol solution ($50\text{ }\mu\text{M}$). As illustrated in Figure 3, compound **3** exhibited four distinct bands across the range of $200\text{--}300\text{ nm}$ with differing levels of intensity. Absorption bands at $205/229\text{ nm}$ ($\epsilon = 47,000/49,600\text{ L}\cdot\text{mol}^{-1}\cdot\text{cm}^{-1}$) and 243 nm ($\epsilon = 26,400\text{ L}\cdot\text{mol}^{-1}\cdot\text{cm}^{-1}$) are attributed to $\pi \rightarrow \pi^*$ transitions of quinoline and 4-chlorobenzoate chromophores, respectively [32,54]. Additionally, the quinoline-containing ester is associated with an absorption band at 278 nm ($\epsilon = 8400\text{ L}\cdot\text{mol}^{-1}\cdot\text{cm}^{-1}$), which is attributed to the $n \rightarrow \pi^*$ transition. As shown in Table 4, the incorporation of the 4-chlorobenzoyl group into 8-hydroxyquinoline (**1**) caused a hypsochromic effect in $\pi \rightarrow \pi^*$ transitions from 208 to 205 nm and 235 to 229 nm , as well as in the $n \rightarrow \pi^*$ transition from 312 to 278 nm . In addition, we observed a strong hypsochromic effect in $\pi \rightarrow \pi^*$ and $n \rightarrow \pi^*$ transitions.

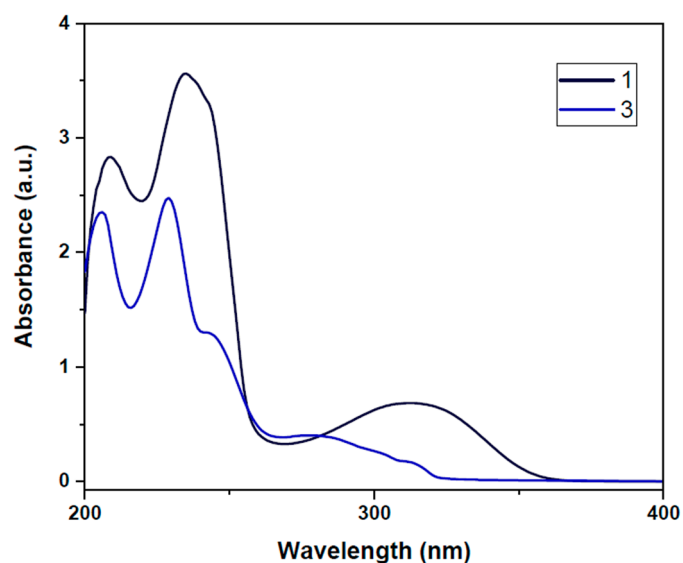


Figure 3. UV-Vis spectra of 8-hydroxyquinoline (1) and quinolin-8-yl 4-chlorobenzoate (3).

Table 4. UV-Vis data of 8-hydroxyquinoline (1) and quinolin-8-yl 4-chlorobenzoate (3) in methanol solution (50 μM).

Compound	λ_{max} (nm)	$\epsilon \times 10^4$ ($\text{L}\cdot\text{mol}^{-1}\cdot\text{cm}^{-1}$)	Assignment
1	208, 235	5.68, 7.12	$\pi \rightarrow \pi^*$
	312	1.36	$n \rightarrow \pi^*$
3	205, 229, 243	4.70, 4.96, 2.64	$\pi \rightarrow \pi^*$
	278	0.84	$n \rightarrow \pi^*$

3.5. TG and DSC Analysis

The thermograms TGA and DSC of compound **3** were recorded separately, as illustrated in Figure 4. The thermal stability of **3** was investigated in a nitrogen atmosphere, with a heating rate of $10\text{ }^\circ\text{C min}^{-1}$ and a gas flow of 25 mL min^{-1} , over a temperature range of 25 to $400\text{ }^\circ\text{C}$. According to the TGA curve, compound **3** exhibits a melting process ranging from 199 to $269\text{ }^\circ\text{C}$. The DSC thermogram of **3** indicates an endothermic peak at $162\text{ }^\circ\text{C}$ ($\Delta H = 120.5\text{ J g}^{-1}$), which coincides with its melting point.

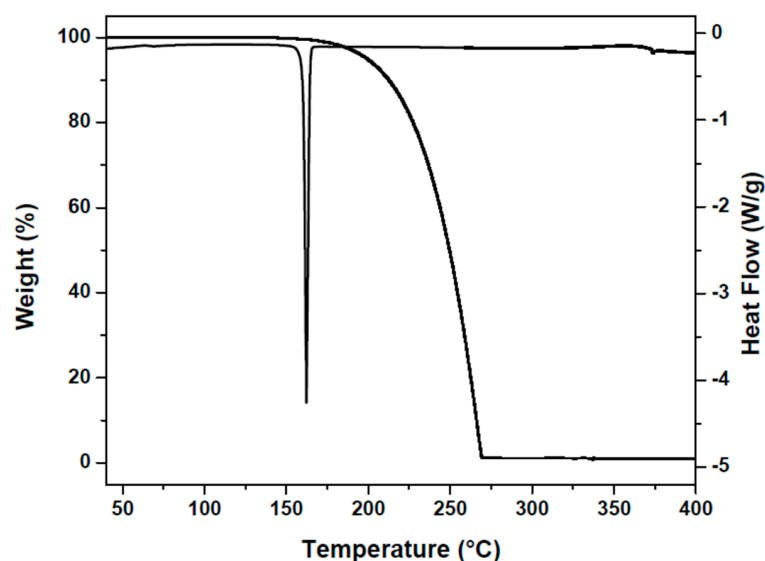


Figure 4. TGA and DSC curves of the quinolin-8-yl 4-chlorobenzoate (3).

3.6. Molecular Structure

CSD database version 5.41 (date of the search: March 2023) using ConQuest software version 2020.1 did not show results for molecules with the exact structural formula. However, a molecular analog named 2-aminoquinolin-8-yl 4-chlorobenzoate was found [58]. Figure 5a shows the molecular structure of **3**. The dihedral angle between the planar fragments that contain the aromatic moieties has a value of 89.30° , suggesting an orthogonal conformation (Figure 5b). It is interesting that the presence of one amine group substituting the quinoline ring in the analog 2-aminoquinolin-8-yl 4-chlorobenzoate distorts this orthogonality, changing the dihedral angle to 72.58 and 79.21° due to the presence of N-H...N hydrogen bonds [58].

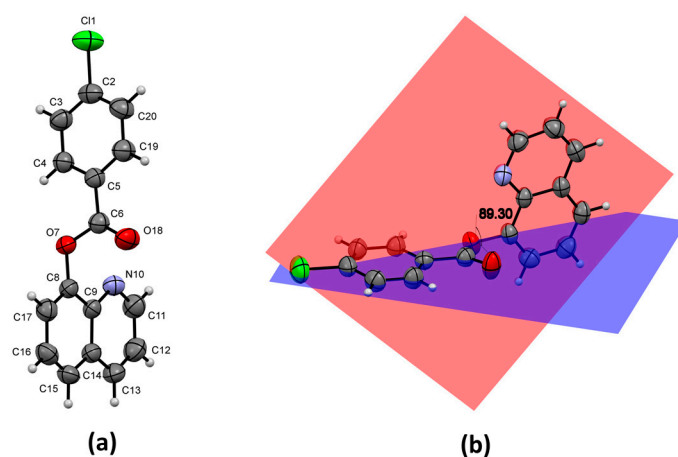


Figure 5. (a) Molecular structure of **3** with anisotropic thermal vibration ellipsoids drawn at the 50% probability level. (b) Dihedral angle between planar fragments in the molecule is shown.

3.7. Supramolecular Structure and Computational Study

In the supramolecular structure of **3**, C3-H3...N10ⁱ hydrogen bonds join pairs of inversion-related molecules (Figure 6a), which are further connected by longer C11-H12...O7ⁱⁱ (symmetry codes: (i) $1 - x, 1 - y, -z$; (ii) $x, y, 1 + z$) hydrogen interactions, forming molecular chains along the [001] direction (Figure 6b and Tables 5 and 6). Inside the chains, the molecular orientation influenced by the C-H... (N, O) hydrogen bonds facilitates the interaction between the chlorine atom and the quinoline ring, forming Cl1... π contacts with distances of $3.7692(12)$ Å and symmetry code $1 - x, 1 - y, -z$ (Figure 6c). Two neighboring chains interact by van der Waals forces and Cl1... π contacts, involving the chlorobenzoate ring of a neighboring molecule, with distances of $3.7631(12)$ Å and symmetry code $x, 1/2 - y, -1/2 + z$ (Figure 6d). In addition, π ... π (symmetry code $2 - x, 1 - y, 1 - z$) and C13-H13...O18ⁱⁱⁱ (symmetry code: (iii) $2 - x, 1 - y, 1 - z$; Tables 5 and 6) interactions help to keep the molecular chains connected through the (001) plane (the plane contained in the *ab* plane) involving the quinoline rings and with distances between π ... π centroids of $3.8859(13)$ Å (Figure 6d and Tables 5 and 6).

Table 5. Selected hydrogen-bond geometry (Å, °) for **3**.

Compound 3				
D-H...A	D-H	H...A	D...A	D-H...A
C3-H3...N10 ⁱ	0.93	2.52	3.431(3)	167
C11-H12...O7 ⁱⁱ	0.93	2.69	3.578(3)	161
C13-H13...O18 ⁱⁱⁱ	0.93	2.78	3.587(3)	145

Symmetry codes: (i) $1 - x, 1 - y, -z$; (ii) $x, y, 1 + z$; (iii) $2 - x, 1 - y, 1 - z$.

Table 6. Selected *CrystalExplorer* CE-B3LYP interaction energies (kJ/mol) for **3**. N is the number of molecules with a molecular centroid-to-centroid distance R (Å). Electron density was calculated using B3LYP/6-31G(d,p) model energies. Symop is the symmetry operation.

N	Symop/Description	R	E _{ele}	E _{pol}	E _{dis}	E _{rep}	E _{tot}
1	1 - x, 1 - y, -z C-H...N, and C11...π	5.62	-20.8	-3.7	-41.7	39.0	-37.0
1	x, y, 1 + z C-H...O	7.40	-7.6	-1.8	-21.3	7.3	-23.4
2	x, 1/2 - y, -1/2 + z C11...π	6.64	-6.6	-2.1	-31.3	16.7	-25.5
1	2 - x, 1 - y, 1 - z C-H...O and π...π	8.78	-17.5	-5.1	-44.4	25.4	-45.3

Scale factors to determine E_{tot}: E_{ele} = 1.05; E_{pol} = 0.74; E_{dis} = 0.87; E_{rep} = 0.61.

The pairwise interaction energies described as electrostatic (E_{ele}), polarization (E_{pol}), dispersion (E_{dis}), and exchange repulsion (E_{rep}) terms show that the crystal packing is controlled mainly by dispersion forces (Table 6). Electrostatic forces are important only in the formation of short hydrogen bonds, which, in the case of **3**, correspond mostly to C3-H3...N10ⁱ (Figure 6a and Tables 5 and 6). However, this contribution in C13-H13...O18ⁱⁱⁱ is also high compared with other interactions in the crystal (Figure 6d and Tables 5 and 6). In addition, Figure 7 shows the energy framework diagrams for pairs of molecules described as having electrostatic (red) and dispersion (green) contributions to the total nearest-neighbor pairwise interaction energies (blue). For compound **3**, the absence of enough short hydrogen bonds induces the crystal to be controlled by dispersion forces, which appear with cylinders of a higher radius compared with the observed contributions from electrostatic cylinders.

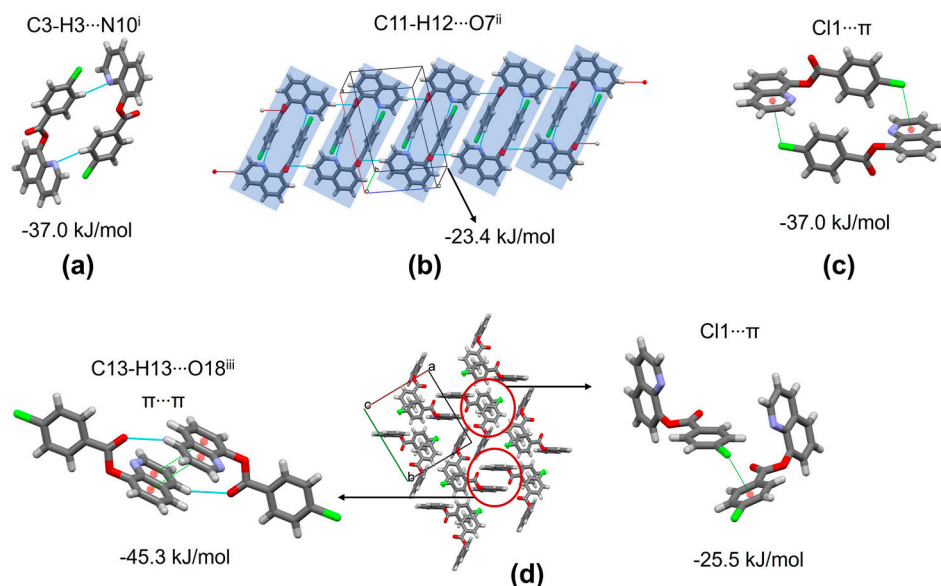


Figure 6. (a) C3-H3...N10ⁱ hydrogen bonds join pairs of inversion-related molecules. (b) C11-H12...O7ⁱⁱ hydrogen bonds helping in the formation of chains in the [001] direction. (c) C11...π contacts. (d) π...π and C13-H13...O18ⁱⁱⁱ interactions helping in the packing. The red circle shows pairwise interaction energies.

C-H...O, C-H...N, π...π, Cl...π and other interactions were analyzed using the *CrystalExplorer* program through Hirshfeld surfaces mapped over d_{norm} [44]. In these maps, interactions smaller than the sum of the van der Waals (Vdw) radii are represented with negative values painted on the surface as red spots. Interactions close to the limit of the Vdw radii are shown in white, and interactions larger are emphasized on the surface in

blue. The intense red spots in the HS (Figure 8) correspond to the shorter interactions C3-H3...N10ⁱ. However, in terms of contributions to the total HS, these hydrogen bonds only provide 6.3%. This is consistent with the low contribution from electrostatic forces to the total packing. Table 6 and Figure 6d show that the highest pairwise interaction is detected for the combination of $\pi\cdots\pi$ (symmetry code $2 - x, 1 - y, 1 - z$) and C13-H13...O18ⁱⁱⁱ interactions, the $\pi\cdots\pi$ contacts being the most important considering the dispersion term in the determination of the total energy (Table 6).

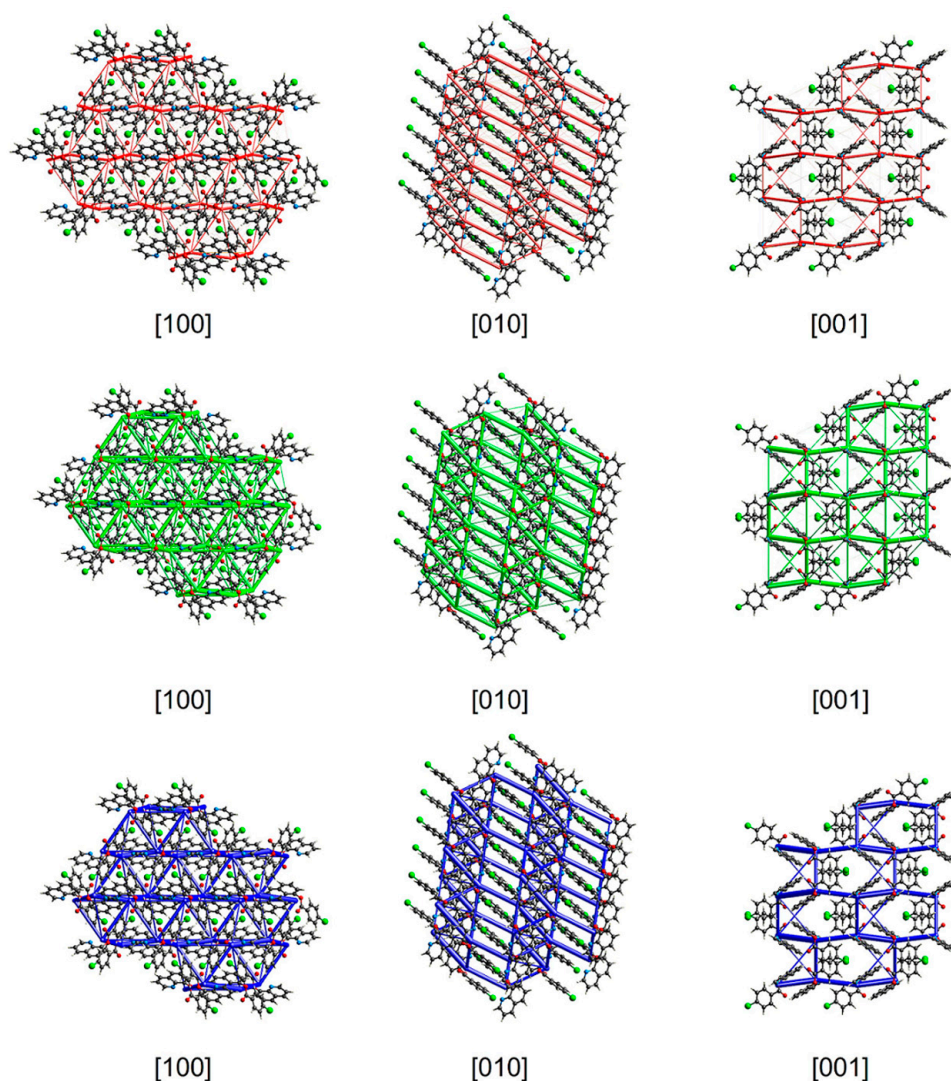


Figure 7. Energy framework diagrams for 3, described as electrostatic (red) and dispersion (green) contributions to the total interaction energies (blue), showing the energetic topology in the packing along [100], [010], and [001] directions. The frameworks are generated within a radius of 10 Å.

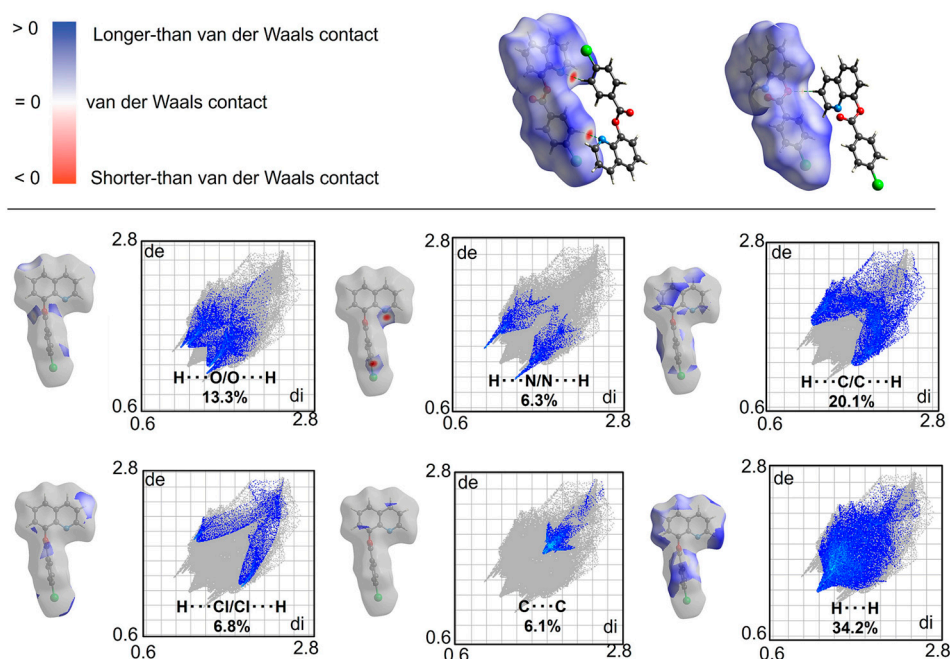


Figure 8. Hirshfeld surfaces mapped over d_{norm} and 2D fingerprint plots including relative contributions (%) to the Hirshfeld surface area for the various close intermolecular contacts for compound **3**.

Molecular electrostatic potentials (ESP) mapped on Hirshfeld surfaces were calculated by the B3LYP method using the 6-31G(d,p) basis set using the crystallographic information [41]. Figure 9 shows the potentials mapped over the range ± 0.05 a.u. [42]. The strongest negative electrostatic potential is observed surrounding the nitrogen atom of the quinoline ring (-1.73 eV) and the oxygen atoms (-1.78 eV) of the ester group (Figure 9). The strongest electropositive electrostatic potential is observed surrounding the aromatic hydrogen atoms of both 4-chlorobenzoate ($+1.42$ eV) and quinoline rings ($+1.02$ and $+1.22$ eV), which explain the short C3-H3 \cdots N10ⁱ hydrogen bonds and the high pairwise interaction energy in the contact comprised by the combination of $\pi\cdots\pi$ and C13-H13 \cdots O18ⁱⁱⁱ interactions (Figure 9). The EPS map over the Cl atom from the 4-chlorobenzoate group suggests the formation of one σ -hole, which could behave as both Lewis acid and base ($+0.016$ and -0.53 eV, respectively). However, the σ -hole does not have enough depth, as observed in the 2-oxo-2*H*-chromen-7-yl 4-chlorobenzoate [59], 4-(4-chlorophenyl)-1-(2-(4-chlorophenyl)-2-ethanone)-1*H*-imidazole [60], and quaternary salts of *N*-halomethylated and non-*N*-halomethylated ammonium [61], which avoid the formation of Cl \cdots Cl interactions. Although these Cl \cdots Cl interactions were not detected in **3**, the negative electrostatic potential over the chlorine atom allows the formation of Cl1 \cdots π interactions (Figure 9).

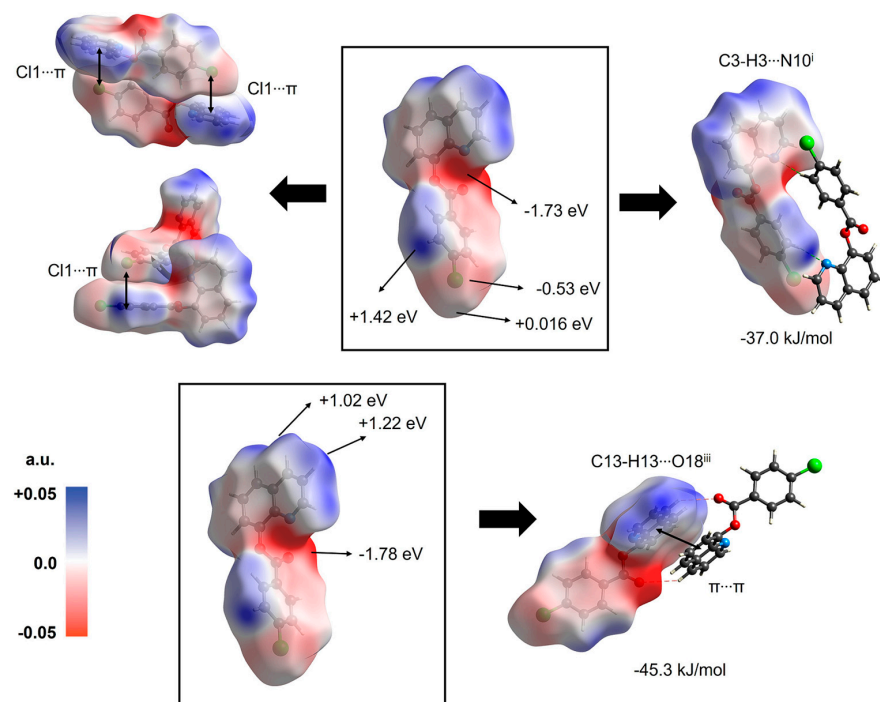


Figure 9. ESPs mapped on Hirshfeld surfaces were mapped over the range -0.05 a.u. (red), through zero (white), to $+0.05$ a.u. (blue) for compound **3**.

In order to acquire a deeper understanding of the reactivity and chemical stability of compound **3**, we calculated the frontier molecular orbital energies (HOMO and LUMO) using the B3LYP method and a 6-31G(d,p) basis set in *CrystalExplorer*. The crystallographic information files (.cif) and TONTO were utilized in this computational study [41]. In Figure 10, the HOMO and LUMO orbitals are extended throughout the entire molecule, except for the 4-chlorophenyl moiety. Based on the calculations, the HOMO and LUMO energy levels were determined to be -6.55 eV and -1.72 eV, respectively. The band gap is a crucial factor in assessing the electrical transport characteristics and chemical reactivity of a molecule [62,63]. The determination of the band gap of compound **3** resulted in 4.83 eV, which suggests a high degree of electron cloud stability and contributes to its observed high chemical stability and low reactivity. These findings are supported by Figure 4, which shows no evidence of decomposition within the temperature range of 25 to 400 °C.

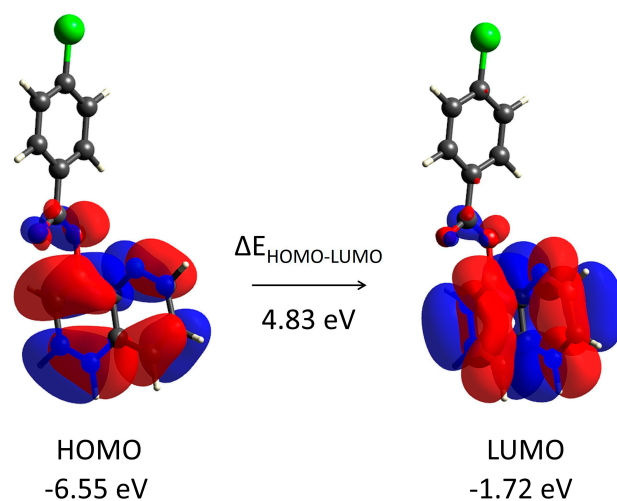


Figure 10. The crystallographic information files (.cif) of compound **3** were used to calculate its HOMO–LUMO energy levels with the B3LYP method and 6-31G(d,p) basis set.

Table 7 shows the values for global reactivity descriptors of compound 3, including its ionization potential (IP), electron affinity (EA), electrophilicity index (ω), chemical potential (μ), electronegativity (χ), and hardness (η). According to Koopmans' theorem, the energy levels of the HOMO and LUMO of common molecules can be correlated to their ionization potential (IP) and electron affinity (EA) values, respectively [64]. The electronegativity (χ) can be calculated based on the average energy values of the HOMO and LUMO, given by the equation $\chi = (\text{IP} + \text{EA})/2$ [62]. The HOMO–LUMO energy gap is associated with the concept of hardness (η), which is a useful indicator of chemical stability [65,66]. The electrophilicity index (ω) is defined as $\omega = \mu^2/2\eta$, where μ represents the chemical potential, which is calculated as $\mu = -(\text{IP} + \text{EA})/2$ [67]. Overall, compound 3 exhibits moderate electrophilicity, as indicated by the electrophilicity index value of 1.77 eV. The chemical potential value of -4.14 eV and the moderate electronegativity of 4.14 eV suggest a moderate ability to attract electrons toward the molecule. The high value of the hardness (η), as indicated by the band gap, suggests that the molecule has a significant resistance to electron transfer, leading to reduced chemical reactivity.

Table 7. HOMO/LUMO energies (eV) and global reactivity descriptors (eV) for compound 3.

Parameters	Compound 3
HOMO Energy	−6.55
LUMO Energy	−1.72
HOMO–LUMO Energy Gap	4.83
Ionization Potential (IP)	6.55
Electron Affinity (EA)	1.72
Electrophilicity Index (ω)	1.77
Chemical Potential (μ)	−4.14
Electronegativity (χ)	4.14
Hardness (η)	4.83

3.8. In Vitro Antitumor Studies

The antitumoral activity of 3 was screened by the NCI (USA) against 60 human cancer cell lines, including Melanoma and Leukemia, and cancers of Breast, Prostate, Renal, Ovarian, Colon, Central nervous system, and non-Small-cell lung. A mean graph showing the growth percentage (G%) of treated cells in contrast to untreated control cells is utilized to report the outcomes of compound 3 (NSC D-832410/1) assessment in the NCI 60-cell panel at a single dose of $10 \mu\text{M}$ [68,69]. Table S1 presents the one-dose mean graph for compound 3 obtained through the NCI 60-cell line screening program. Lethality is indicated by a negative value in the growth inhibition percentage (GI%), whereas a decrease in the growth percentage (G%) results in an increase in the growth inhibition percentage ($\text{GI}\% = 100 - \text{G}\%$) [68,69]. Table 8 displays the most important anticancer results for compound 3. Despite the low activity in 3, the findings can provide valuable insights into how chemical structure and anticancer activity are connected.

Table 8. Remarkable anticancer results for compound 3.

Mean Growth Percentage	Most Sensitive Cell Lines	Growth Inhibition Percentage (GI%)
102.4	HOP-92 (non-Small-cell lung cancer)	6.2
	EKVX (non-Small-cell lung cancer)	6.4
	UO-31 (Renal cancer)	18.1
	SK-MEL-2 (Melanoma)	−13.9
	OVCAR-3 (Ovarian cancer)	−15.4
	BT-549 (Breast cancer)	−16.4

Compound 3 shows low anticancer activity against HOP-92 and EKVX non-Small-cell lung cancer cell lines with a growth inhibition percentage (GI%) of 6.2% and 6.4%,

respectively (Table 8 and Table S1). However, the most significant anticancer effect is observed in the UO-31 Renal cancer cell line with a GI% of 18.1%. Despite the compound's low anticancer activity, it is noteworthy for its high selectivity towards the UO-31 Renal cancer cell line. Overall, anticancer studies of quinoline derivatives have shown different mechanisms of action involving the inhibition of topoisomerase, tyrosine kinases, tubulin polymerization, carbonic anhydrase, telomerase, quinone reductase 2 (QR2), farnesyltransferase, proteasome, poly(ADP-ribose) polymerase-1 (PARP-1), histone deacetylase (HDAC), nuclear factor kappa B (NF-kB), heat shock protein 90 (Hsp90), histone acetyltransferase (HAT), as well as DNA intercalating agents, iron chelators, free-radical regulators, Bcl-2 family protein modulators, among others [11–16]. In particular, quinoline-based drugs available on the market or in the clinical trial phase mainly act as inhibitors of protein kinases, topoisomerases, or directly intercalating DNA [12]. Notably, multi-targeted tyrosine kinase inhibitors, such as cabozantinib and lenvatinib, are utilized in the treatment of advanced renal cell carcinoma (RCC) [12,17,19]. Thereby, the moderate activity of **3** against the UO-31 Renal cancer cell line could be explained by its behavior as a potential inhibitor of protein kinases.

4. Conclusions

We report the utilization of the Monowave 50 reactor for the triethylamine-mediated synthesis of ester **3** in high yield under mild reaction conditions. This procedure stands out for its brief reaction duration, operational simplicity, and clean reaction profile. The anticancer evaluation, IR, UV–Vis spectra, thermal behavior, and crystal structure of compound **3** introduce information that is missing from the literature. X-ray diffraction analyses of **3** show that C–H \cdots N, C–H \cdots O, Cl \cdots π , and $\pi\cdots\pi$ interactions are present in the supramolecular structure. The molecular conformation of **3** in the solid state presents an orthogonal orientation between quinoline and 4-chlorobenzoate rings. CE-B3LYP interaction energies show that dispersion forces act in a higher proportion than electrostatic forces to assemble the crystal, which can be explained by the absence of enough short hydrogen bonds. Moreover, electrostatic potentials suggest the formation of σ -holes over the Cl atoms to behave as both Lewis acid and base; however, Cl \cdots Cl interactions are absent due to the slight depth of σ -holes. Quantum chemical descriptors and global reactivity descriptors were examined using the B3LYP method with the 6–31G(d,p) basis set implemented in *CrystalExplorer*. Finally, quinolin-8-yl 4-chlorobenzoate (**3**) displayed low activity against HOP-92, EK VX non-Small-cell lung, and UO-31 Renal cancer cell lines with a growth inhibition percentage (GI%) ranging from 6.2% to 18.1%. Even compounds with low activity can contribute to a better understanding of how chemical structure and biological activity are connected.

Supplementary Materials: The following supporting information can be downloaded at: <https://www.mdpi.com/article/10.3390/cryst13040694/s1>. Figure S1: EI-MS spectrum for compound **3**; Figure S2: FT-IR spectrum for compound **3**; Figure S3: Expansion of the IR spectrum for compound **3**; Figure S4: UV–Vis spectra for compounds **1** and **3**; Figure S5: ^1H NMR spectrum for compound **3**; Figure S6: $^{13}\text{C}\{^1\text{H}\}$ NMR and DEPT-135 spectra for compound **3**; Figure S7: HSQC 2D C–H correlation spectrum for compound **3**; Figure S8: HMBC 2D C–H correlation spectrum for compound **3**; Figure S9: COSY 2D C–H correlation spectrum for compound **3**; Table S1: Mean growth, %GI, and lethality values displayed by the tested compound **3** against 60 NCI human cancer cell lines at 10 μM ; Table S2: Experimental bond lengths (\AA) and bond/valence angles ($^\circ$) obtained from single crystal X-ray measurements for compound **3**.

Author Contributions: Investigation, data curation, writing—original draft preparation, J.-C.C.; data curation, writing—original draft preparation, D.B.; investigation, data curation, writing—original draft preparation, M.A.M. All authors have read and agreed to the published version of the manuscript.

Funding: This research received no external funding.

Data Availability Statement: The data presented in this study are available in this article.

Acknowledgments: D.B. and J.-C.C. thank the Dirección de Investigaciones at the Universidad Pedagógica y Tecnológica de Colombia for financial support (project number: SGI-3470). M.A.M. acknowledges support from the Facultad de Ciencias at the Universidad de los Andes (project number: FAPA-P18.160422.043). We are grateful to the National Cancer Institute (NCI, USA) for performing the anticancer evaluation of compound **3**. We also acknowledge Universidad del Valle and Universidad de Alcalá for acquiring EI-MS and NMR spectra, respectively. The authors thank Anton Paar Colombia S.A.S. for loaning the reactor Monowave 50 (Anton Paar GmbH).

Conflicts of Interest: The authors declare no conflict of interest.

References

1. Marella, A.; Tanwar, O.P.; Saha, R.; Ali, M.R.; Srivastava, S.; Akhter, M.; Shaquiquzzaman, M.; Alam, M.M. Quinoline: A versatile heterocyclic. *Saudi Pharm. J.* **2013**, *21*, 1–12. [[CrossRef](#)]
2. Insuasty, B.; Montoya, A.; Becerra, D.; Quiroga, J.; Abonia, R.; Robledo, S.; Vélez, I.D.; Upegui, Y.; Nogueras, M.; Cobo, J. Synthesis of novel analogs of 2-pyrazoline obtained from [(7-chloroquinolin-4-yl)amino]chalcones and hydrazine as potential antitumor and antimalarial agents. *Eur. J. Med. Chem.* **2013**, *67*, 252–262. [[CrossRef](#)]
3. Teng, P.; Li, C.; Peng, Z.; Vanderschouw, A.M.; Nimmagadda, A.; Su, M.; Li, Y.; Sun, X.; Cai, J. Facilely accessible quinoline derivatives as potent antibacterial agents. *Bioorg. Med. Chem.* **2018**, *26*, 3573–3579. [[CrossRef](#)] [[PubMed](#)]
4. Musiol, R. Quinoline-based HIV integrase inhibitors. *Curr. Pharm. Des.* **2013**, *19*, 1835–1849. [[CrossRef](#)] [[PubMed](#)]
5. Vandekerckhove, S.; Tran, H.G.; Desmet, T.; D’hooghe, M. Evaluation of (4-aminobutyloxy)quinolines as a novel class of antifungal agents. *Bioorg. Med. Chem. Lett.* **2013**, *23*, 4641–4643. [[CrossRef](#)]
6. Zajdel, P.; Partyka, A.; Marciniak, K.; Bojarski, A.J.; Pawlowski, M.; Wesolowska, A. Quinoline- and isoquinoline-sulfonamide analogs of aripiprazole: Novel antipsychotic agents? *Future Med. Chem.* **2014**, *6*, 57–75. [[CrossRef](#)] [[PubMed](#)]
7. Ghanim, A.M.; Girgis, A.S.; Kariuki, B.M.; Samir, N.; Said, M.F.; Abdelnaser, A.; Nasr, S.; Bekheit, M.S.; Abdelhameed, M.F.; Almalki, A.J.; et al. Design and synthesis of ibuprofen-quinoline conjugates as potential anti-inflammatory and analgesic drug candidates. *Bioorg. Chem.* **2022**, *119*, 105557. [[CrossRef](#)] [[PubMed](#)]
8. Jarvis, B.; Markham, A. Montelukast: A review of its therapeutic potential in persistent asthma. *Drugs* **2000**, *59*, 891–928. [[CrossRef](#)]
9. Loiseau, P.M.; Balaraman, K.; Barratt, G.; Pomel, S.; Durand, R.; Frézard, F.; Figadère, B. The potential of 2-substituted quinolines as antileishmanial drug candidates. *Molecules* **2022**, *27*, 2313. [[CrossRef](#)] [[PubMed](#)]
10. Muruganatham, N.; Sivakumar, R.; Anbalagan, N.; Gunasekaran, V.; Leonard, J.T. Synthesis, anticonvulsant and antihypertensive activities of 8-substituted quinoline derivatives. *Biol. Pharm. Bull.* **2004**, *27*, 1683–1687. [[CrossRef](#)]
11. Afzal, O.; Kumar, S.; Haider, M.R.; Ali, M.R.; Kumar, R.; Jaggi, M.; Bawa, S. A review on anticancer potential of bioactive heterocycle quinoline. *Eur. J. Med. Chem.* **2015**, *97*, 871–910. [[CrossRef](#)]
12. Musiol, R. An overview of quinoline as a privileged scaffold in cancer drug discovery. *Expert Opin. Drug Discov.* **2017**, *12*, 583–597. [[CrossRef](#)] [[PubMed](#)]
13. Jain, S.; Chandra, V.; Jain, P.K.; Pathak, K.; Pathak, D.; Vaidya, A. Comprehensive review on current developments of quinoline-based anticancer agents. *Arab. J. Chem.* **2019**, *12*, 4920–4946. [[CrossRef](#)]
14. Mohamed, M.F.A.; Abu-Rahma, G.E.-D.A. Molecular targets and anticancer activity of quinoline–chalcone hybrids: Literature review. *RSC Adv.* **2020**, *10*, 31139–31155. [[CrossRef](#)] [[PubMed](#)]
15. Dorababu, A. Report on recently (2017–20) designed quinoline-based human cancer cell growth inhibitors. *ChemistrySelect* **2020**, *5*, 13902–13915. [[CrossRef](#)]
16. Ilakiyalakshmi, M.; Napoleon, A.A. Review on recent development of quinoline for anticancer activities. *Arab. J. Chem.* **2022**, *15*, 104168. [[CrossRef](#)]
17. Bowles, D.W.; Kessler, E.R.; Jimeno, A. Multi-targeted tyrosine kinase inhibitors in clinical development: Focus on XL-184 (cabozantinib). *Drugs Today* **2011**, *47*, 857–868. [[CrossRef](#)]
18. Rossari, F.; Minutolo, F.; Orciuolo, E. Past, present, and future of Bcr-Abl inhibitors: From chemical development to clinical efficacy. *J. Hematol. Oncol.* **2018**, *11*, 84. [[CrossRef](#)]
19. Cabanillas, M.E.; Habra, M.A. Lenvatinib: Role in thyroid cancer and other solid tumors. *Cancer Treat. Rev.* **2016**, *42*, 47–55. [[CrossRef](#)]
20. Venditto, V.J.; Simanek, E.E. Cancer therapies utilizing the camptothecins: A review of the in vivo literature. *Mol. Pharm.* **2010**, *7*, 307–349. [[CrossRef](#)]
21. Oliveri, V.; Vecchio, G. 8-Hydroxyquinolines in medicinal chemistry: A structural perspective. *Eur. J. Med. Chem.* **2016**, *120*, 252–274. [[CrossRef](#)] [[PubMed](#)]
22. Saadeh, H.A.; Sweidan, K.A.; Mubarak, M.S. Recent advances in the synthesis and biological activity of 8-hydroxyquinolines. *Molecules* **2020**, *25*, 4321. [[CrossRef](#)] [[PubMed](#)]
23. Gupta, R.; Luxami, V.; Paul, K. Insights of 8-hydroxyquinolines: A novel target in medicinal chemistry. *Bioorg. Chem.* **2021**, *108*, 104633. [[CrossRef](#)] [[PubMed](#)]

24. Jiang, H.; Taggart, J.E.; Zhang, X.; Benbrook, D.M.; Lind, S.E.; Ding, W.-D. Nitroxoline (8-hydroxy-5-nitroquinoline) is more a potent anti-cancer agent than clioquinol (5-chloro-7-iodo-8-quinoline). *Cancer Lett.* **2011**, *312*, 11–17. [CrossRef] [PubMed]
25. Ding, W.-D.; Liu, B.; Vaught, J.L.; Yamauchi, H.; Lind, S.E. Anticancer activity of the antibiotic clioquinol. *Cancer Res.* **2005**, *65*, 3389–3395. [CrossRef] [PubMed]
26. Joaquim, A.R.; Gionbelli, M.P.; Gosmann, G.; Meneghello Fuentefria, A.; Silva Lopes, M.; Fernandes de Andrade, S. Novel antimicrobial 8-hydroxyquinoline-based agents: Current development, structure–activity relationships, and perspectives. *J. Med. Chem.* **2021**, *64*, 16349–16379. [CrossRef] [PubMed]
27. Chabukswar, A.R.; Kuchekar, B.S.; Jagdale, S.C.; Lokhande, P.D.; Chabukswar, V.V.; Shisodia, S.U.; Mahabal, R.H.; Londhe, A.M.; Ojha, N.S. Synthesis and evaluation of analgesic, anti-asthmatic activity of (*E*)-1-(8-hydroxyquinolin-7-yl)-3-phenylprop-2-en-1 ones. *Arab. J. Chem.* **2016**, *9*, 704–712. [CrossRef]
28. Pearce, D.A.; Jotterand, N.; Carrico, I.S.; Imperiali, B. Derivatives of 8-hydroxy-2-methylquinoline are powerful prototypes for Zinc sensors in biological systems. *J. Am. Chem. Soc.* **2001**, *123*, 5160–5161. [CrossRef]
29. Mameli, M.; Aragoni, M.C.; Arca, M.; Caltagirone, C.; Demartin, F.; Farruggia, G.; De Filippo, G.; Devillanova, F.A.; Garau, A.; Isaia, F.; et al. A selective, nontoxic, OFF–ON fluorescent molecular sensor based on 8-hydroxyquinoline for probing Cd²⁺ in living cells. *Chem.–Eur. J.* **2010**, *16*, 919–930. [CrossRef] [PubMed]
30. Bell, J.; Samb, I.; Toullec, P.Y.; Mongin, O.; Blanchard-Desce, M.; Michelet, V.; Leray, I. Ultra-sensitive and selective Hg²⁺ chemosensors derived from substituted 8-hydroxyquinoline analogues. *New J. Chem.* **2014**, *38*, 1072–1078. [CrossRef]
31. Gao, L.-B.; Kang, W.-K.; Yan, S.-H.; Yang, C.-P. Studies of substituents impact on the photophysical properties of 8-hydroxyquinoline derivatives. *Heteroat. Chem.* **2016**, *27*, 54–62. [CrossRef]
32. Zhang, H.; Han, L.-F.; Zachariasse, K.A.; Jiang, Y.-B. 8-Hydroxyquinoline benzoates as highly sensitive fluorescent chemosensors for transition metal ions. *Org. Lett.* **2005**, *7*, 4217–4220. [CrossRef] [PubMed]
33. Hu, S.; Jin, Y.; Liu, Y.; Ljungman, M.; Neamati, N. Synthesis and mechanistic studies of quinolin-chlorobenzothioate derivatives with proteasome inhibitory activity in pancreatic cancer cell lines. *Eur. J. Med. Chem.* **2018**, *158*, 884–895. [CrossRef]
34. Maddocks, C.J.; Aathimanikandan, S.V.; Richardson, J.; Ruble, J.C. Quinolin-8-yl formate: A new option for small-scale carbonylation reactions in microwave reactors. *Synlett* **2020**, *31*, 1608–1612. [CrossRef]
35. For Details of the Monowave 50 Instruments. Available online: <https://www.anton-paar.com/co-es/productos/detalles/reactor-de-sintesis-monowave-50/> (accessed on 15 December 2022).
36. CrysAlisPro 1.171.39.46e, Rigaku Oxford Diffraction, 2018. Available online: <https://www.rigaku.com/products/crystallography/crysalis> (accessed on 9 January 2023).
37. Palatinus, L.; Chapuis, G. SUPERFLIP—A computer program for the solution of crystal structures by charge flipping in arbitrary dimensions. *J. Appl. Crystallogr.* **2007**, *40*, 786–790. [CrossRef]
38. Sheldrick, G.M. Crystal structure refinement with SHELXL. *Acta Crystallogr. Sect. C Struct. Chem.* **2015**, *71*, 3–8. [CrossRef]
39. Macrae, C.F.; Bruno, I.J.; Chisholm, J.A.; Edgington, P.R.; McCabe, P.; Pidcock, E.; Rodriguez-Monge, L.; Taylor, R.; van de Streek, J.; Wood, P.A. Mercury CSD 2.0—New features for the visualization and investigation of crystal structures. *J. Appl. Crystallogr.* **2008**, *41*, 466–470. [CrossRef]
40. Spackman, M.A.; Jayatilaka, D. Hirshfeld surface analysis. *CrystEngComm* **2009**, *11*, 19–32. [CrossRef]
41. Jayatilaka, D.; Grimwood, D.J.; Lee, A.; Lemay, A.; Russel, A.J.; Taylor, C.; Wolff, S.K.; Cassam-Chenai, P.; Whitton, A. TONTO—A System for Computational Chemistry. 2005. Available online: <http://hirshfeldsurface.net> (accessed on 9 January 2023).
42. Spackman, M.A.; McKinnon, J.J.; Jayatilaka, D. Electrostatic potentials mapped on Hirshfeld surfaces provide direct insight into intermolecular interactions in crystals. *CrystEngComm.* **2008**, *10*, 377–388. [CrossRef]
43. Mackenzie, C.F.; Spackman, P.R.; Jayatilaka, D.; Spackman, M.A. CrystalExplorer model energies and energy frameworks: Extension to metal coordination compounds, organic salts, solvates and open-shell systems. *IUCr* **2017**, *4*, 575–587. [CrossRef]
44. Turner, M.J.; McKinnon, J.J.; Wolff, S.K.; Grimwood, D.J.; Spackman, P.R.; Jayatilaka, D.; Spackman, M.A. CrystalExplorer17, 2017, University of Western Australia. Available online: <http://hirshfeldsurface.net/> (accessed on 9 January 2023).
45. Corma, A.; Iborra, S.; Velty, A. Chemical routes for the transformation of biomass into chemicals. *Chem. Rev.* **2007**, *107*, 2411–2502. [CrossRef]
46. Brown, D.G.; Boström, J. Analysis of past and present synthetic methodologies on medicinal chemistry: Where have all the new reactions gone? *J. Med. Chem.* **2016**, *59*, 4443–4458. [CrossRef] [PubMed]
47. Obermayer, D.; Znidar, D.; Glotz, G.; Stadler, A.; Dallinger, D.; Kappe, C.O. Design and performance validation of a conductively heated sealed-vessel reactor for organic synthesis. *J. Org. Chem.* **2016**, *81*, 11788–11801. [CrossRef]
48. Tobiszewski, M.; Namieśnik, J.; Pena-Pereira, F. Environmental risk-based ranking of solvents using the combination of a multimedia model and multi-criteria decision analysis. *Green Chem.* **2017**, *19*, 1034–1042. [CrossRef]
49. Silverstein, R.M.; Webster, F.X.; Kiemle, D.J.; Bryce, D.L. *Spectrometric Identification of Organic Compounds*, 8th ed.; Wiley: Hoboken, NJ, USA, 2014.
50. Fernandes, R.F.; Stroppa, P.H.F.; Ferreira, G.R.; da Silva, A.D.; Edwards, H.G.M.; de Oliveira, L.C.F. Vibrational spectroscopic study of some quinoline derivatives. *Vib. Spectrosc.* **2016**, *86*, 128–133. [CrossRef]
51. Krishnakumar, V.; Ramasamy, R. DFT studies and vibrational spectra of isoquinoline and 8-hydroxyquinoline. *Spectrochim. Acta A Mol. Biomol. Spectrosc.* **2005**, *61*, 673–683. [CrossRef] [PubMed]

52. Bahgat, K.; Ragheb, A.G. Analysis of vibrational spectra of 8-hydroxyquinoline and its 5,7-dichloro, 5,7-dibromo, 5,7-diiodo and 5,7-dinitro derivatives based on density functional theory calculations. *Cent. Eur. J. Chem.* **2007**, *5*, 201–220. [[CrossRef](#)]
53. Saral, A.; Sudha, P.; Muthu, S.; Sevvanthi, S.; Sangeetha, P.; Selvakumari, S. Vibrational spectroscopy, quantum computational and molecular docking studies on 2-chloroquinoline-3-carboxaldehyde. *Heliyon* **2021**, *7*, e07529. [[CrossRef](#)]
54. Castillo, J.-C.; Martínez, J.J.; Becerra, D.; Rojas, H.; Macías, M.A. Obtaining (5-formylfuran-2-yl)methyl 4-chlorobenzoate through an esterification of 5-hydroxymethylfurfural: Interesting achiral molecule crystallizing in a Sohncke $P2_12_12_1$ space group. *J. Mol. Struct.* **2022**, *1268*, 133713. [[CrossRef](#)]
55. Xiao, L.; Liu, Y.; Xiu, Q.; Zhang, L.; Guo, L.; Zhang, H.; Zhong, C. Novel polymeric metal complexes as dye sensitizers for dye-sensitized solar cells based on polythiophene containing complexes of 8-hydroxyquinoline with Zn(II), Cu(II) and Eu(III) in the side chain. *Tetrahedron* **2010**, *66*, 2835–2842. [[CrossRef](#)]
56. Janghour, M.; Amini, M.M. Effect of zinc oxide doping on electroluminescence and electrical behavior of metalloporphyrin-doped samarium complex. *J. Electron. Mater.* **2018**, *47*, 2761–2767. [[CrossRef](#)]
57. Vivas-Reyes, R.; Núñez-Zarur, F.; Martínez, E. Electronic structure and reactivity analysis for a set of Zn-chelates with substituted 8-hydroxyquinoline ligands and their application in OLED. *Org. Electron.* **2008**, *9*, 625–634. [[CrossRef](#)]
58. Park, Y.; Fei, X.; Yuan, Y.; Lee, S.; Hur, J.; Park, S.J.; Jung, J.-K.; Seo, S.-Y. Chemoselective acylation of 2-amino-8-quinolinol in the generation of C2-amides or C8-esters. *RSC Adv.* **2017**, *7*, 41955–41961. [[CrossRef](#)]
59. Salinas-Torres, A.; Jiménez, E.; Becerra, D.; Martínez, J.J.; Rojas, H.; Castillo, J.-C.; Macías, M.A. Synthesis, anticancer evaluation, thermal and X-ray crystallographic analysis of 2-oxo-2H-chromen-7-yl 4-chlorobenzoate using a conductively heated sealed-vessel reactor. *J. Mol. Struct.* **2022**, *1274*, 134414. [[CrossRef](#)]
60. García-Olave, M.; Elejalde-Cadena, N.R.; Portilla, J.; Macías, M.A. C–H \cdots X (X = F, Cl) and Cl \cdots Cl halogen-mediated interactions driving the crystal packing in *N*-substituted 4-arylimidazoles. *J. Mol. Struct.* **2023**, *1272*, 134181. [[CrossRef](#)]
61. Molina Giraldo, D.A.; Ríos Vásquez, L.A.; Toscano, R.A.; Ocampo-Cardona, R.; Gomez-Peña, J.J.; Macías, M.A. Synthesis and crystallographic study of six quaternary salts of *N*-halomethylated and non-*N*-halomethylated ammonium: Importance of C–H \cdots X (X = F, I) and I \cdots I–halogen interactions in the supramolecular structures. *J. Mol. Struct.* **2023**, *1271*, 133962. [[CrossRef](#)]
62. Nataraj, A.; Balachandran, V.; Karthick, T. Molecular orbital studies (hardness, chemical potential, electrophilicity, and first electron excitation), vibrational investigation and theoretical NBO analysis of 2-hydroxy-5-bromobenzaldehyde by density functional method. *J. Mol. Struct.* **2013**, *1031*, 221–233. [[CrossRef](#)]
63. Geerlings, P.; De Proft, F.; Langenaeker, W. Conceptual density functional theory. *Chem. Rev.* **2003**, *103*, 1793–1874. [[CrossRef](#)]
64. Antonijevic, I.S.; Janjic, G.V.; Milic, M.; Zaric, S.D. Preferred geometries and energies of sulfur–sulfur interactions in crystal structures. *Cryst. Growth Des.* **2016**, *16*, 632–639. [[CrossRef](#)]
65. Politzer, P.; Abu-Awwad, F. A comparative analysis of Hartree-Fock and Kohn-Sham orbital energies. *Theor. Chem. Acc.* **1998**, *99*, 83–87. [[CrossRef](#)]
66. Mulliken, R.S. A new electroaffinity scale; together with data on valence states and on valence ionization potentials and electron affinities. *J. Chem. Phys.* **1934**, *2*, 782. [[CrossRef](#)]
67. Parr, R.G.; von Szentpaly, L.; Liu, S. Electrophilicity index. *J. Am. Chem. Soc.* **1999**, *121*, 1922–1924. [[CrossRef](#)]
68. Serrano-Sterling, C.; Becerra, D.; Portilla, J.; Rojas, H.; Macías, M.; Castillo, J.-C. Synthesis, biological evaluation and X-ray crystallographic analysis of novel (*E*)-2-cyano-3-(het)arylacrylamides as potential anticancer agents. *J. Mol. Struct.* **2021**, *1244*, 130944. [[CrossRef](#)]
69. Abonia, R.; Insuasty, D.; Castillo, J.; Insuasty, B.; Quiroga, J.; Noguera, M.; Cobo, J. Synthesis of novel quinoline-2-one based chalcones of potential antitumor activity. *Eur. J. Med. Chem.* **2012**, *57*, 29–40. [[CrossRef](#)]

Disclaimer/Publisher’s Note: The statements, opinions and data contained in all publications are solely those of the individual author(s) and contributor(s) and not of MDPI and/or the editor(s). MDPI and/or the editor(s) disclaim responsibility for any injury to people or property resulting from any ideas, methods, instructions or products referred to in the content.